Universal ventricular coordinates: A generic framework for describing position within the heart and transferring data

Jason Bayer, Anton J Prassl, Ali Pashaei, Juan F. Gómez, Antonio Frontera, Aurel Neic, Gernot N Plank, Edward Vigmond

Medical Image Analysis 45 (2018) 83–93

Contents lists available at ScienceDirect

Medical Image Analysis

journal homepage: www.elsevier.com/locate/media

Universal ventricular coordinates: A generic framework for describing position within the heart and transferring data

Jason Bayer[a,b], Anton J. Prassl[c], Ali Pashaei[a,b], Juan F. Gomez[a,b], Antonio Frontera[a,d], Aurel Neic[c], Gernot Plank[c], Edward J. Vigmond[a,b,*]

[a] LIRYC Electrophysiology and Heart Modeling Institute, Bordeaux Fondation, avenue du Haut-Lévèque, Pessac 33600, France
[b] IMB Bordeaux Institute of Mathematics, University of Bordeaux, 351 cours de la Libération, Talence 33405, France
[c] Gottfried Schatz Research Center, Biophysics, Medical University of Graz, Neue Stiftingtalstrasse 6, 8010 Graz, Austria
[d] Department of Electrophysiology, Hôpital Haut Lévèque, 1 avenue Magellan, Pessac 33100 France

ARTICLE INFO

Article history:
Received 10 July 2017
Revised 16 January 2018
Accepted 22 January 2018
Available online 2 February 2018

Keywords:
Mapping
Coordinates
Volumetric meshes
Deformation

ABSTRACT

Being able to map a particular set of cardiac ventricles to a generic topologically equivalent representation has many applications, including facilitating comparison of different hearts, as well as mapping quantities and structures of interest between them. In this paper we describe Universal Ventricular Coordinates (UVC), which can be used to describe position within any biventricular heart. UVC comprise four unique coordinates that we have chosen to be intuitive, well defined, and relevant for physiological descriptions. We describe how to determine these coordinates for any volumetric mesh by illustrating how to properly assign boundary conditions and utilize solutions to Laplace's equation. Using UVC, we transferred scalar, vector, and tensor data between four unstructured ventricular meshes from three different species. Performing the mappings was very fast, on the order of a few minutes, since mesh nodes were searched in a KD tree. Distance errors in mapping mesh nodes back and forth between meshes were less than the size of an element. Analytically derived fiber directions were also mapped across meshes and compared, showing $< 5°$ difference over most of the ventricles. The ability to transfer gradients was also demonstrated. Topologically variable structures, like papillary muscles, required further definition outside of the UVC framework. In conclusion, UVC can aid in transferring many types of data between different biventricular geometries.

1. Introduction

The ventricles of mammalian hearts share many common characteristics. These include a biventricular geometry, Purkinje system (PS), and helical myocardial fiber orientation (Streeter et al., 1969). They also express electrical heterogeneity with respect to transmural (Lou et al., 2011; Sabir et al., 2007), apicobasal (Janse et al., 2012), and left-right gradients (Pandit et al., 2011; Volders et al., 1999).

It is recognized that describing such scalar, vector, and tensor data on a generic heart framework is important, especially in the clinical context. This prompted the American Heart Association to define a standard 17 sector map over a decade ago (Cerqueira et al., 2002). However, it can be difficult to accurately transfer high-resolution data and compare results between vastly different heart geometries. This difficulty arises from the highly variable size and relative proportion of hearts within the same species or between different species.

Modern day methods for mapping ventricular data between hearts are namely based on large deformation diffeomorphic metric mapping (LDDMM) applied to anatomical data from magnetic resonance imaging (MRI) and computed tomography scans (Beg et al., 2005). LDDMM has shown success for mapping myocardial fiber orientation (Vadakkumpadan et al., 2012) and anatomical positioning (Miller et al., 2014) between hearts. However, several drawbacks have limited LDDMM's widespread use to a large array of other problems. For example, LDDMM works directly with voxelized image data and is computationally demanding (hours) when the template and target hearts are of significantly different resolu-

* Corresponding author.
E-mail addresses: jason.bayer@ihu-liryc.fr (J. Bayer), anton.prassl@medunigraz.at (A.J. Prassl), ali.pashaei@u-bordeaux.fr (A. Pashaei), juan.gomez@ihu-liryc.fr (J.F. Gomez), a.frontera@gmail.com (A. Frontera), aurel.neic@medunigraz.at (A. Neic), gernot.plank@medunigraz.at (G. Plank), edward.vigmond@u-bordeaux.fr (E.J. Vigmond).

https://doi.org/10.1016/j.media.2018.01.005

tions, particularly if at least one of the data sets has a submillimeter resolution. This makes transferring large quantities of data between histology, imaging, and computer models extremely daunting. Furthermore, unstructured meshes, which are extensively used for electromechanical modeling, need to be converted back and forth between an image stack format. This significantly increases the storage and processing time for LDDMM, as well as introduces sampling errors at the surfaces of the mesh.

We propose a novel global positioning system for three-dimensional biventricular heart geometries to overcome the limitations of LDDMM. Accordingly, we define a set of generic ventricular coordinates to define position within any biventricular heart that takes only minutes to formulate on <12 central processing units (CPU), even for mesh resolutions at the submillimeter scale that require significant input/output. The method also works equally well for regular or irregular meshes.

To help foster more expansive data sharing, the coordinates are intuitive so that experimentalists can easily estimate them for their data, which also facilitates transferring experimental data directly to computer modeling studies. Furthermore, the coordinates vary smoothly in space so that they can be used as arguments to functions that assign myocardial properties based on position. Finally, despite geometries which can be quite different, subjectivity is minimized when assigning the coordinates so that interobserver variability is reduced.

To develop our UVC, we build upon aspects from previous computational cardiac modeling studies. To determine position in the left ventricular (LV) geometry for mechanical simulations, Costa et al. (1996) used prolate spheroidal coordinates. For the purpose of assigning action potential heterogeneity in a biventricular mesh for electrocardiogram genesis, Potse et al. (2006) used minimal distance parameterizations between epicardial and endocardial surfaces to define the myocardial transmural direction, and Keller et al. (2012) extended this approach to define the apicobasal direction. Bayer et al. (2012) parameterized the same transmural and apicobasal directions in biventricular geometries for assigning rule-based myocardial fiber orientation, but they determined these directions more accurately from solutions to Laplace's equation instead of minimal distance. Paun et al. (2017) also followed a Laplace approach for mapping complex endocardial anatomy. Despite these developments, none provide a complete parameterization for arbitrary biventricular geometries, particularly for the septum and its junction with the LV, right ventricle (RV), and apex.

In this article, we first present the rationale and methods for determining UVC for arbitrary volumetric heart meshes. We then demonstrate how to use UVC for transferring scalar, vector, and tensor data between different biventricular meshes. To evaluate the algorithm's performance, we analyze errors associated with the transformation process. The results from this new approach show great promise for its widespread use to determine unique positioning in the heart and facilitate the transfer of data between hearts.

2. Methods

2.1. UVC rationale

Position is described within arbitrary ventricles by a combination of four parameters called Universal Ventricular Coordinates (UVC). As mentioned in the introduction, the rationale for UVC is based on how clinical and experimental studies define spatial data within the ventricles. Accordingly, the first coordinate of UVC, $\mathfrak{z}$, represents the distance traveled along the long axis of the ventricles from the apex to the base. The second coordinate of UVC, ρ, is the distance from the endocardium to epicardium, i.e. transmurality. The third coordinate of UVC, ϕ, is the circumferential distance around the long axis of the LV and RV. The ϕ is necessary to distinguish between the posterior and anterior regions of the ventricles in $\mathfrak{z}$ and ρ. The final coordinate, ν, distinguishes between the LV and RV for the other three coordinates of UVC. In the following sections, necessary user inputs and UVC are discussed in detail utilizing the biventricular human mesh described in Moreno et al. (2011), Bayer et al. (2016).

2.2. User inputs for UVC

To compute UVC, the user must first provide the following inputs: (i) a single epicardial apex surface point; (ii) a single LV endocardial surface point; (iii) a single RV septal surface point; and (iv) the surface points representing the ventricular base at the atrioventricular junction. The rest of the algorithm is fully automatic, with only one tolerance (T_{SEPT}) to adjust for optimal results. T_{SEPT} defines the RV septal surface and is described later in more detail.

With the user inputs above, the following surfaces are obtained to compute UVC in a biventricular mesh.

1. Base
2. Epicardium
3. LV endocardium
4. RV endocardium
5. RV septum

The process of obtaining each surface is as follows. For a volumetric mesh, the entire surface is known by identifying all element faces not shared by another tissue element. On this surface, the user defines the base, which then leaves three distinct isolated regions: the epicardium; LV endocardium; and RV endocardium. The epicardial surface is identified by finding the surface containing the epicardial apex point (input by the user). The LV endocardium is identified by finding the endocardial surface containing the LV endocardial surface point (input by the user) with the third remaining surface labeled as RV endocardium. The RV endocardium is further subdivided into its septal and free wall endocardial regions using the change in the surface normal at the interface between the RV septum and endocardium. More specifically, starting from the user input septal node on the RV surface, the algorithm defines each connected element as endocardium and then grows the region by looking at surface normals. If the normal of a surface element under consideration does not differ by more than the tolerance T_{SEPT} from its neighboring element, it is added to the region. A T_{SEPT} of 0.05 for the dot product of neighboring normals is used for all meshes in this study. In the case the resolution of the mesh is too low to detect prominent changes in surface normals at the junction of the RV septum with the free wall, manual segmentation would be straightforward given the oversimplified geometry at such resolutions. Manual intervention may also be used for the base input if it is difficult to define automatically using simple numerical approaches.

2.3. Separating the ventricles at the LV-RV junction

To facilitate the computation of UVC, the LV, RV, and LV-RV junction domains are identified in the biventricular geometry. Accordingly, the boundary conditions shown in Fig. 1A are assigned to the surfaces of the biventricular mesh, where ϕ =0 on the LV endocardium, ϕ =0.5 on the RV septum, and ϕ =1 on the RV endocardium. Solving Laplace's equation using these Dirichlet boundary conditions gives the solution shown in Fig. 1B. Using this scalar field, the LV is defined by all scalar values ≤ 0.5 (Fig. 1C) and the RV by all scalar values >0.5 (Fig. 1D).

2.4. Apicobasal coordinate - $\mathfrak{z}$

The apicobasal direction from the apex to base of the ventricles is represented with the coordinate $\mathfrak{z}$ following the approach

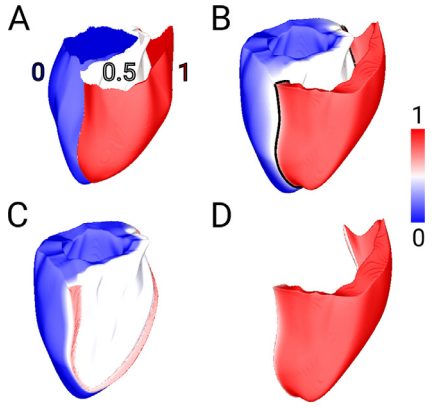

Fig. 1. Separation of the LV and RV. **A:** Three Dirichlet boundary conditions applied to the LV endocardium (0.0), RV septum (0.5), and RV endocardium (1.0) of the biventricular human mesh. **B:** The solution to Laplace's equation with the boundary conditions in A. The LV-RV interface is defined by the isoline shown at 0.51. **C:** The separated LV. **D:** The separated RV.

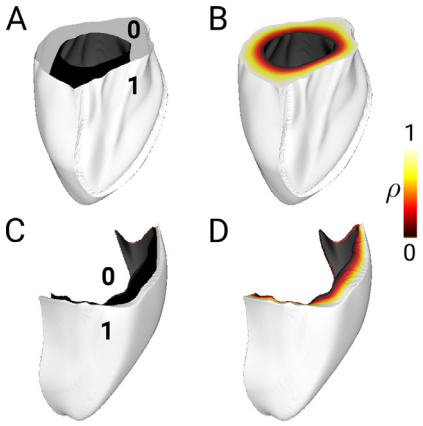

Fig. 3. Transmural coordinate - ρ. Two Dirichlet boundary conditions applied to the endocardium (0.0) and epicardium (1.0) of the LV (**A**) and RV (**C**) of the biventricular human mesh. The solution to Laplace's equation with the boundary conditions in A and C to obtain ρ in the LV (**B**) and RV (**D**), respectively.

by Bayer et al. (2012). Accordingly, $\mathfrak{z}$ is defined as the solution to Laplace's equation with Dirichlet boundary conditions of 0 applied to the apex and 1 to the base (Fig. 2A). All meshes should share the same location for the ventricular apex to avoid error in $\mathfrak{z}$. For example, the RV apex and LV apex for all hearts are not always in the same plane that is perpendicular to the long axis of the heart. Thus, an apical boundary condition is placed at the LV-RV junction to ensure a consistent $\mathfrak{z}$ for all LV and RV apical orientations within biventricular meshes. To obtain this point at the LV-RV junction, the minimal distance between the LV apex point (input by the user) and the epicardial surface of the RV apex in Fig. 1D is determined. Then the closest point on each the LV and RV endocardial surfaces to this new LV-RV apical point on the epicardium is found. Lastly, two vectors are defined by connecting the epicardial LV-RV apical point to each of the LV and RV endocardial points. Apical boundary nodes are identified by finding all mesh nodes that have a distance perpendicular to either of these two vectors with a magnitude less than 1.5 times the average edge length for all elements in the biventricular mesh. The 1.5-fold threshold for labeling apical nodes guarantees a smooth apical boundary for meshes with irregular elements. The apical boundary is shown in Fig. 2A for the biventricular human mesh.

To ensure the solution for $\mathfrak{z}$ varies smoothly and evenly from the apex to the base, the geodesic approach by Paun et al. (2017) is used to normalize $\mathfrak{z}$. With this approach, the shortest geodesic distance from the apex to the base is determined (Fig. 2B). The initial Laplace solution in Fig. 2B is then sampled along this geodesic as a function of normalized distance to generate a mapping from the Laplace solution to the normalized distance as shown in Fig. 2C.

2.5. Transmural coordinate - ρ

The coordinate ρ represents the distance from the endocardium to epicardium. Since the interventricular septum can be more typical of LV than RV electrophysiology (Morita et al., 2007), ρ is solved separately in the LV and RV with the septum as an extension to the LV free wall. As a result, ρ is 0 on the LV and non-septal RV endocardial surfaces, and is 1 on the epicardial and septal RV endocardial surfaces. The Dirichlet boundary conditions for these surfaces on the LV and RV are shown in Fig. 3A and C. The solutions to Laplace's equation with these boundary conditions to obtain ρ for the LV and RV are shown in Fig. 3B and D.

2.6. Rotational coordinate - ϕ

The coordinate ϕ represents the circumferential rotation around the long axes of the LV and RV. In our algorithm, ϕ is computed separately in the LV and RV by solving Laplace's equation with the Dirichlet boundary conditions shown in Fig. 4A for ϕ in the LV (Fig. 4B), and the boundary conditions shown in Fig. 4C for ϕ in the RV (Fig. 4D). In the LV of Fig. 4A, ϕ rotates from $+\pi$ in the LV wall (magenta) to $+\pi/2$ at the outer (orange) and $+\pi/2.5$ at the inner (yellow) surfaces of the anterior LV-RV junction, and then to 0 at the middle of the septum (green). The inverse occurs for the posterior region of the ventricles from 0 at the septum to $-\pi$ in the LV free wall. In the RV, the ϕ solution in Fig. 4D rotates from $+\pi/2$ at the anterior surface of the LV-RV junction (orange) to $-\pi/2$ at the posterior surface of the LV-RV junction (blue) in Fig. 4C. With this representation for ϕ, ventricular points in the anterior region of the ventricles are defined at $\phi > 0$ and

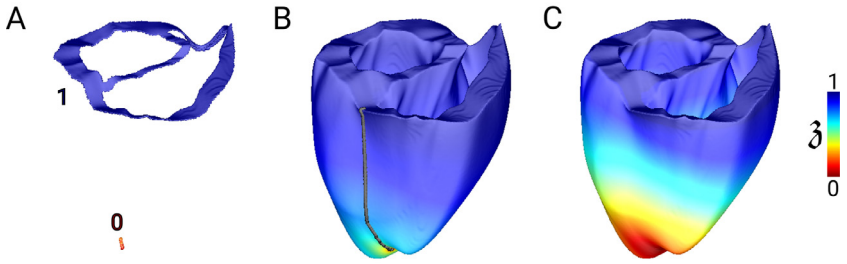

Fig. 2. Apicobasal coordinate -$\mathfrak{z}$. **A:** Dirichlet boundary conditions applied to the apex (0.0) and base (1.0) of the biventricular human mesh. **B:** The initial solution to Laplace's equation with the boundary conditions in A to obtain $\mathfrak{z}$. The dark line is the geodesic for the minimal distance traveled from the ventricular apex to base. **C:** The normalized $\mathfrak{z}$ using the distance traveled along the geodesic.

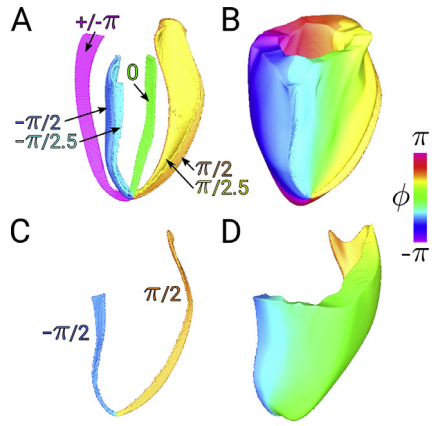

Fig. 4. Rotational coordinate - ϕ. **A:** Dirichlet boundary conditions applied to the LV at the LV wall ($\pm\pi$), outer surfaces of the LV-RV junction ($\pm\pi/2$), inner surfaces of the LV-RV junction ($\pm\pi/2.5$), and septum (0). **B:** The solution to Laplace's equation with the boundary conditions in A to obtain ϕ in the LV. **C:** Dirichlet boundary conditions applied to the RV at the surfaces of the LV-RV junction ($\pm\pi/2$). **D:** The solution to Laplace's equation with the boundary conditions in C to obtain ϕ in the RV.

in the posterior at $\phi \leq 0$. The septum is defined for all LV points with $-\pi/2.5 < \phi < +\pi/2.5$. The LV-RV junction is defined for all anterior LV points with $+\pi/2.5 < \phi < +\pi/2$, and all posterior RV points with $-\pi/2 < \phi < -\pi/2.5$.

Obtaining the seven LV boundaries in Fig. 4A requires two intermediate steps. In step one, the boundaries midway in the septum and LV free wall are determined using the LV-RV junction. Thus, these boundaries align ϕ in the LV with respect to the LV-RV junction. By setting the anterior boundary of the LV-RV junction to +1 and the posterior boundary of the LV-RV junction to -1, as shown in Fig. 5A, the solution to Laplace's equation with these boundaries conditions is shown in Fig. 5B. For this solution, all mesh elements that intersect zero are identified and divided into septal and LV wall regions at the LV-RV apical boundary shown in Fig. 2A. The septal division serves as the ϕ=0 boundary, the LV free wall division at 0 serves as the $\phi = +\pi$ boundary, and the element nodes touching the free wall boundary at zero with nodes <0 in the solution of Fig. 5B serve as the $\phi = -\pi$ boundary in Fig. 4A.

Step two requires the determination of boundaries at the LV-RV interface that ensure ϕ changes smoothly around the LV, and that define the septum according to the unique LV-RV junction of each biventricular mesh. Specifically, the endocardial surface in Fig. 5E is obtained by determining the average scalar value in Fig. 5D for the inner anterior and posterior boundaries of Fig. 5A. Then the endocardial boundary surface is defined by identifying all endocardial surface nodes between these two average values in Fig. 5D, and the epicardial surface is defined by identifying all epicardial surface nodes between the inner anterior and posterior boundaries. By setting these two endocardial and epicardial boundaries to +1, and all other surface nodes of the LV to -1, the solution in Fig. 5F at 0 defines the $\phi \pm \pi/2.5$ surfaces in Fig. 4A, with the posterior region being the cyan $-\pi/2.5$ surface and the anterior region being the yellow $+\pi/2.5$ surface. This same approach was performed to obtain the $\pm\pi/2$ surfaces in Fig. 4A. The only difference is that the endocardial and epicardial surfaces in Fig. 5G to obtain the solution in Fig. 5H is obtained using the outer LV-RV junction boundaries in Fig. 5A.

The two boundaries at $\pm\pi/2$ in Fig. 4C are obtained by setting the surfaces at the LV-RV junction that do not belong to the RV endocardial or epicardial surfaces to $+\pi/2$ for nodes anterior the RV apex, and to $-\pi/2$ for nodes posterior the LV-RV apex. The values of $\pm\pi/2$ are chosen to be consistent with the range of π in the LV free wall.

Table 1
Finite element mesh statistics. Length (L) is measured along the long axis, and width (W) is the maximum dimension along the short axis. $\overline{V_e}$ = average element volume and $\overline{l_e}$ = average edge length. The predominant element type is either tetrahedral (Tet) or hexahedral (Hex).

Species	#nodes 1,000 s	#elements 1,000 s	L cm	W cm	$\overline{V_e}$ nL	$\overline{l_e}$ μm	Element type
Rabbit-1	1,049	5,931	3.18	2.92	1.23	246	Tet
Rabbit-2	548	3,073	2.78	2.92	2.23	279	Tet
Canine	26.7	149	5.66	6.55	464	1749	Tet
Human	2,423	29,290	10.0	10.9	77.9	472	Hex
OxRabHi	4,283	24,100	2.93	2.36	0.231	129	Tet
OxRabLo	4,234	24,348	2.93	2.36	0.229	128	Tet

2.7. Transventricular coordinate - ν

The coordinate ν determines whether the other three coordinates are within the LV or RV of the biventricular mesh. Accordingly, ν is set to -1 in the LV (Fig. 6A) for ≤ 0.5 in Fig. 1B, and to +1 in the RV (Fig. 6B) at > 0.5 in Fig. 1B.

2.8. Test meshes

In addition to the high resolution human biventricular mesh (Bayer et al., 2016) used above to illustrate the various coordinates of our UVC algorithm, we test our algorithm in volumetric unstructured finite element meshes for two rabbit hearts of different resolution (Vetter and McCulloch, 1998) and a canine heart (http://gforge.icm.jhu.edu/gf/project/dtmri_data_sets/). These additional meshes, shown in Fig. 7, allow for testing on a wide range of cardiac geometries varying in size and resolution. See Table 1 for further details.

2.9. Specialized cardiac structures

Several cardiac structures exist which do not easily fall into the framework described above due to their highly variable geometry and/or location. These structures include the trabeculae and the aortic, mitral, pulmonary, and tricuspid valve openings at the base of the ventricles. Methods to deal with them when present in biventricular meshes are described below and demonstrated on an anatomically precise, high resolution mesh of the rabbit ventricles (Plank et al., 2009; Bishop and Plank, 2012).

2.9.1. Trabeculae

When viewed at high resolution, the endocardia are quite rough despite being depicted as smooth in most meshes used for numerical simulations. Simply assigning the endocardia with a uniform boundary condition to determine ρ will fail as most of the trabecular surface will be assigned the same value, leading to a uniform ρ coordinate value within the trabeculae. To overcome this, we propose to first create a low precision mesh which assigns an endocardial surface which "fills in" the spaces between the trabeculae to produce a smooth surface. UVC are solved on the less precise mesh and then the values are projected back onto the detailed mesh. There will now be holes in the UVC space corresponding to spaces between the trabeculae. This scheme allows mapping trabeculae from one heart to the smooth endocardia of a different heart. An example of assigning ρ on trabeculae is shown in Fig. 8 using the high precision Oxford rabbit heart (OxRabHi) constructed at 125 μm resolution (Bishop et al., 2010). A low precision version of the mesh (OxRabLo) was built at the same resolution but without trabeculation.

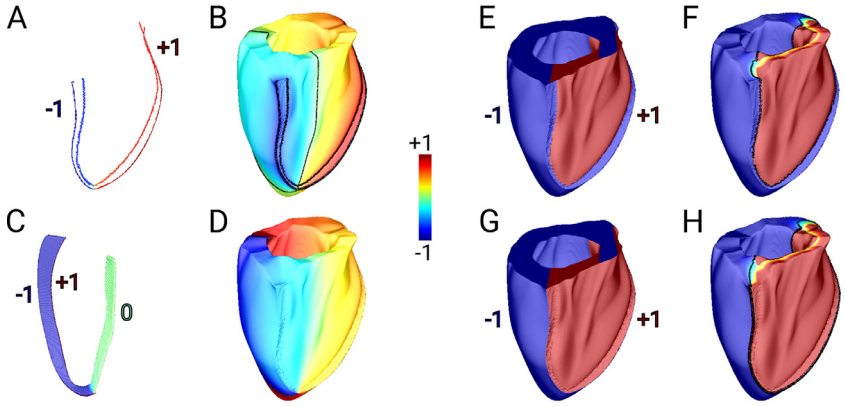

Fig. 5. Methods to obtain boundary conditions for ϕ in the LV. **A:** Dirichlet boundary conditions on the boundaries of the LV-RV junction. **B:** Solution to Laplace's equation with the boundary conditions in A (isolines at LV-RV junction) to obtain the boundary conditions in **C** at the isoline shown at 0. **D:** The solution to Laplace's equation with the Dirichlet boundary conditions in C to obtain the inner and outer endocardial boundary conditions of 1 in **E,G**. **F,H:** The solution to Laplace's equation with the boundary conditions in E,G to obtain the inner and outer surfaces of the LV-RV junction for ϕ for the isolines shown at 0.

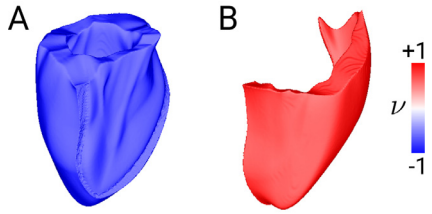

Fig. 6. Transventricular coordinate - v. **A:** LV at v =-1. **B:** RV at v =+1.

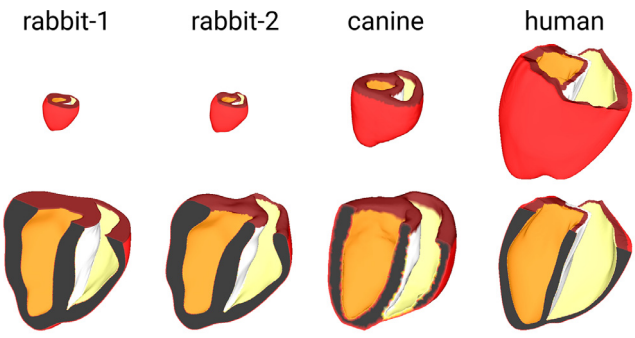

Fig. 7. Geometries used for intermesh transfers. **Top**: Epicardial view showing relative sizes. **Bottom**: Cut view showing cavities with all hearts scaled to the same size. Colors indicate the LV endocardium (orange), septum (white), RV endocardium (yellow), base (burgundy), and epicardium (red). (For interpretation of the references to color in this figure legend, the reader is referred to the web version of this article.)

2.9.2. Valves

Heart valves are present at the base of the ventricles. When included in a biventricular mesh, the UVC algorithm can be extended to handle these openings by identifying the surface elements of the mesh for the mitral, aortic, pulmonary, and tricuspid valve openings (Fig. 9A). These four boundaries then serve as the base boundary conditions for the UVC algorithm outlined in the previous sections.

To define UVC in the bridges between the valves that are not part of the septum or the RV and LV free walls, continuous rings are manually placed around the base of each bridge (Fig. 9B). Then $\mathfrak{z}$ (Fig. 9C) is solved for in these bridges by setting $\mathfrak{z}$ to 1.0 in the ring that touches the free wall, and to 1.25 in the ring that touches the septum. The ϕ (Fig. 9D) in these bridges is determined by setting the mitral and tricuspid regions to $-\pi$, and the aortic and pulmonary regions to $+\pi$. The bridge solutions for $\mathfrak{z}$ and ϕ are

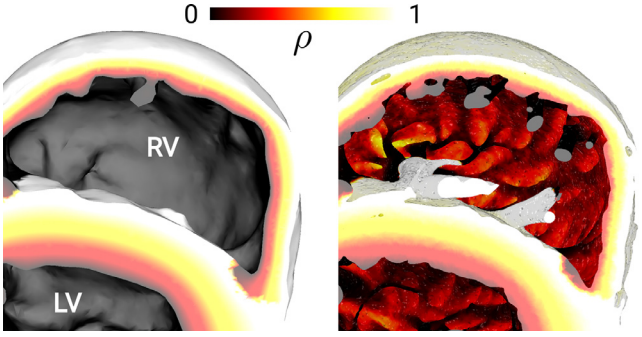

Fig. 8. Assigning ρ to a trabeculated mesh. **Left**: Low precision OxRabLo mesh on which the coordinate ρ was solved for according to Section 2.5. **Right**: ρ projected onto the high precision OxRabHi mesh. The superior view of the bottom half of the heart is the same for both meshes. In the RV of the OxRabHi mesh, papillary muscles can be seen emanating from the wall. Red and yellow represent pockets in the endocardium, with black being the same depth as the surface on the left. The cut edge of the detailed RV free wall illustrates how the depth is related to ρ on the surface. (For interpretation of the references to color in this figure legend, the reader is referred to the web version of this article.)

then combined with the UVC for rest of the ventricles. Therefore, when $\mathfrak{z} > 1.0$, UVC are exclusive to these intravalvular regions.

3. Mapping information between different biventricular meshes

The mapping between different biventricular meshes begins with a source finite element mesh with nodes expressed in Cartesian coordinates and UVC, and data at each node. A target point expresses a position in space, in either coordinate system, at which data is sought. The finite element bounding the target point is identified and the nodal data interpolated to the target point. Details for the different data types follow.

3.1. Implementation

The mapping software is two separate codes linked by a shell script. The purpose of the first code is to identify the elements in the mesh which potentially enclose a given point, based on distance to the element center. It is written in Python utilizing the SciPy (Jones et al., 2001) cKDTree module, which includes an optimized KD tree algorithm (Maneewongvatana and Mount, 2001) to find the nearest points in space. It offers excellent performance

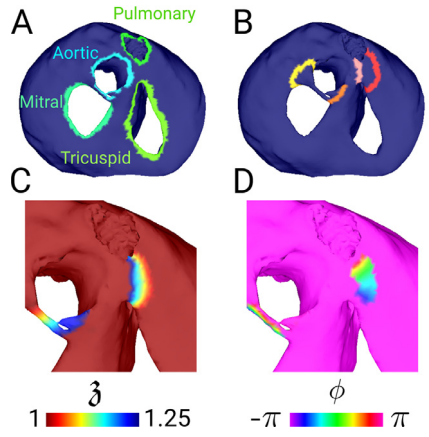

Fig. 9. Assigning UVC to the OxRabLo ventricular mesh containing valve openings. **A:** The mesh elements labeled around each valve opening. **B:** User chosen circular rings around the junctions of the LV and RV bridges in between the valves. **C:** The solution for $\mathfrak{z}$ in the LV and RV bridges. **D:** The solution for ϕ in the LV and RV bridges.

since construction is $O(n\log n)$ and searches are $O(\log n)$. Searching distance in UVC space is distorted compared to Cartesian space since the apicobasal distance of the heart is ten times larger than the transmural thickness, yet $\mathfrak{z}$ and ρ both cover the range [0,1]. Likewise, ϕ and ν span different ranges with different physical dimensions. Therefore, a simple scaling is performed along each axis of the UVC to equalize the importance of the coordinates when calculating distance, d:

$$d = \sqrt{s_{\mathfrak{z}}^2(\mathfrak{z}_1 - \mathfrak{z}_2)^2 + s_{\rho}^2(\rho_1 - \rho_2)^2 + (\phi_1 - \phi_2)^2} \tag{1}$$

where s_η is the scaling factor for axis η.

The UVC search space is first divided into left and right spaces based on the ν coordinate, thereby reducing the search to three dimensions ($\mathfrak{z}$, ρ, and ϕ). Special care is taken when searching near the branch cut of the ϕ coordinate, since $-\pi$ is at the same position as π. Points near the branch cut are duplicated in the node list with ϕ offset by a value of 2π. For example, point a at -0.99π is duplicated as 1.01π so that point b at 0.98π is recognized as being in close proximity of point a. The search program finds the nearest finite element centers to the points of interest.

The second program, written in C++, reads in the lists of nearby elements found by the first program, and determines which element actually encloses the target points. Linear interpolation is then performed within the finite element. For points not contained within an element, an inverse distance weighting function is used based on the distances from the nodes defining the nearest element.

All code is ran on desktop machines equipped with 3.0 GHz Intel processors and 32 GB of RAM. Laplacian solves are performed using the CARP software with algebraic multigrid preconditioning (Plank et al., 2007). A public version of this software, referred to as *CARPentry*, is available to install at https://carpentry.medunigraz.at/carputils/cme-installation.html.

3.2. Scalar

In biventricular meshes, scalar field data such as activation times, action potential duration, etc., are important parameters for investigating the electrical behavior of the heart. Target points are expressed in UVC and data is interpolated onto them.

3.3. Structural

Accurately representing structural data in biventricular meshes is essential so that computer simulations of cardiac electrical activity corroborate experimental and clinical data. For example, accurately representing the PS in biventricular meshes is necessary to simulate physiologic activation patterns that trigger the muscle contractions which pump blood throughout the body. Within mammalian hearts, the initial cable of the PS runs from the bundle of His through the ventricular septum before exiting and covering the endocardia (ρ =0 on the LV and RV encodardia, and ρ =1 on the RV septum). The PS at the endocardia then penetrate a species dependent distance into the myocardium to form Purkinje-muscular junctions that transfer electrical pulses from the PS to the myocardium. Since the human PS cannot be imaged *in vivo*, which is also time consuming and expensive to quantify *ex vivo*, it is more efficient to map preexisting PS networks defined within large mammals to biventricular meshes.

Mapping structural data is similar to scalar data. The structure to be transferred is expressed in UVC and becomes the target points in the destination mesh. Instead of scalar data, the Cartesian coordinates of the nodes are interpolated.

3.4. Vector

In mammalian ventricles, the macroscopic 3D structure of ventricular myocytes resembles a helical fiber orientation (Streeter et al., 1969). Cardiac fiber orientation helps govern the anisotropic propagation of electrical waves in the ventricles and is important for mechanical aspects of contraction (Eriksson et al., 2013). Therefore, it is important to accurately incorporate cardiac fiber orientation into biventricular meshes. Accordingly, directional tissue anisotropy is incorporated into each finite element of a biventricular mesh as a 3D tensor.

Transferring this vector data is performed by constructing a local orthonormal basis at each target point based on UVC, interpolating the vector field to this point, and then projecting the desired vector onto this basis. This is a pull operation which represents the vector in the UVC frame. Note, pull operations interpolate nodal data values and possibly F to interior points, while push operations interpolate F to the target interior point. While the gradients of three coordinates, e.g. $\mathfrak{z}$, ρ, and ϕ, span $\mathbb{R}^3$, they are nonorthogonal and require computation of the contravariant vectors for any operations. To avoid this, we compute an orthonormal basis by setting the first direction, $\hat{e}_0$, to be along the direction grad $\mathfrak{z}$, i.e. the gradient of $\mathfrak{z}$ with respect to Cartesian coordinates. Away from the apex, this is similar to the long axis. It is the least noisy and most independent direction. Other directions could be chosen for $\hat{e}_0$ with slightly worse results. The next direction, $\hat{e}_1$, is the normalized component of the gradient of ρ orthogonal to $\hat{e}_0$:

$$\hat{e}_1 = \frac{\text{grad}\,\rho - <\text{grad}\,\rho, \hat{e}_0>\hat{e}_0}{|\,\text{grad}\,\rho - <\text{grad}\,\rho, \hat{e}_0>\hat{e}_0|} \tag{2}$$

Finally, $\hat{e}_2 = \hat{e}_0 \times \hat{e}_1$. Thus, any vector $\bar{A}$ can be expressed by $\bar{A} = \Sigma_0^2 <\bar{A}, \hat{e}_i>\hat{e}_i$. The second step of the transfer requires constructing the local orthonormal bases at the target points in the destination mesh and multiplying the bases by the coefficients found in the first step.

Transferring orientations is a special case of transferring vectors. Unlike vectors, fiber orientations have no sense, so a flip of 180° has no effect, and consequently, two fiber orientations can differ by no more than 90°. Thus, care must be taken when adding fiber orientations together during averaging to enforce the preceding rule.

3.5. Gradient

It is often of interest to transfer gradient data between meshes, such as that pertaining to the velocity of electrical waves propagating throughout the myocardium. By treating the coordinate frame of UVC as a reference configuration, it is then possible to determine the deformation gradient, F, between the UVC and Cartesian coordinates:

$$F = \begin{pmatrix} \partial x/\partial \mathfrak{z} & \partial x/\partial \rho & \partial x/\partial \phi \\ \partial y/\partial \mathfrak{z} & \partial y/\partial \rho & \partial y/\partial \phi \\ \partial z/\partial \mathfrak{z} & \partial z/\partial \rho & \partial z/\partial \phi \end{pmatrix} \tag{3}$$

Quantities are pulled to UVC from the Cartesian reference frame, and pushed from the UVC frame to the Cartesian reference frame. The gradient can be transferred using the identity

$$\mathrm{Grad}\, A(\mathfrak{z}, \rho, \phi) = F^T \,\mathrm{grad}\, a(x, y, z) \tag{4}$$

where Grad is the gradient with respect to UVC. The entries of F can be determined directly by numerically finding the gradients of the Cartesian coordinates with respect to the UVC on the volumetric mesh. Alternatively, we find the components of F^{-1} directly by computing the gradient of the UVC on the Cartesian grid. Gradients are determined by fitting the shape functions over each finite element in the mesh based on nodal values, and then differentiating shape functions to compute the gradient within the element. Nodal gradients are then computed by averaging the attached elemental gradients weighted by their respective volumes. Regardless of whether grad or Grad is computed, calculations involving ϕ need extra attention because of the discontinuity introduced by the branch cut.

Similar to vectors, transfers between grids is a two step operation. The first step is to pull to UVC, and the second to push back to Cartesian coordinates. Given a source mesh with F_S and a destination mesh with F_D as computed at the same UVC point in the meshes,

$$\mathrm{grad}\, a(x_D, y_D, z_D) = F_D^{-T} F_S^T \,\mathrm{grad}\, a(x_S, y_S, z_S) \tag{5}$$

4. Results

4.1. Searching in UVC space

The accuracy of searching in UVC space was addressed. The ϕ was unchanged while $\mathfrak{z}$ was scaled in the range 1–6, and $\rho \in \{0.1, 0.2, .333, 0.5, 0.75, 1\}$. Node locations from the mesh were searched using element centers as described above. The search was successful if the node location was identified as being inside an element which comprised the node. For each mesh, the minimum number of failures was found within the studied range of scaling values. Results are shown in Fig. 10. The more finely discretized meshes performed better, being successful $>99\%$ of the time. The canine mesh was the coarsest, tending to have a higher error rate than the rabbit meshes. The error rate with the human mesh was the most sensitive to scaling within the range studied. With no scaling, 10% of the nodes were mislocated but this dropped to less than 1% as $\mathfrak{z}$ scaling was increased. Part of the reason for this different behaviour may be because it was a hybrid hexahedron dominant mesh. For simplicity, to determine if a point was inside a hexahedron, the algorithm assumed planar faces which was not necessarily the case, possibly resulting in false negatives. Over most of the range studied, the rabbit meshes were correct $>99\%$ of the time. Errors primarily occurred along the LV-RV interface, especially near the base, and near the apex.

The scaling pair which minimized the error over all meshes was 3 for $\mathfrak{z}$ and 0.33 for ρ. Given that the $\mathfrak{z}$ dimension physically spans a length 10 times that spanned by ρ in Cartesian space, a factor of 9 in scaling is reasonable for the coordinate. The ϕ has a ratio of distance spanned in centimeters to the coordinate range of around 5 at the base for the human mesh, while for $\mathfrak{z}$ it is 10. Thus scaling $\mathfrak{z}$ by 2 would equalize the search sensitivity for these coordinates. However, this distance-to-range ratio decreases for ϕ as the apex is approached, meaning that the optimal scaling would have to increase, thus explaining the empirically found value of 3. The length and width ratio are fairly constant for all hearts so this scaling applies to all models. The scaling of (3, 0.3) was used for all subsequent mappings. Results using the global scaling are seen in Table 2. Timing information for the method is shown in Table 3.

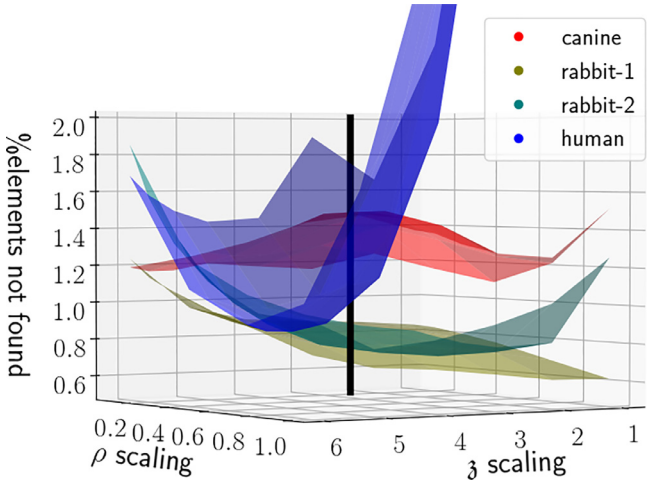

Fig. 10. Percentage of incorrectly assigned nodes as a function of coordinate scaling. Each surface represents the percentage of nodes located in an element to which they did not belong for each mesh. The black vertical line represents the optimal scaling taken over all meshes.

Table 2
Accuracy in finding nodes within the correct elements. $\bar{d}$ is the average distance from the node to a permissible element center for mislocated nodes.

Mesh	#incorrect	$\bar{d}$ µm
Human	21,770	1,050
Rabbit-1	4,666	592
Rabbit-2	8,551	470
Canine	379	4,268

Table 3
Timing for operations in seconds. Transfers mapped from nodal values to element centers. One time operations are listed in the top portion of the table.

Operation	Canine	Human
Landmark selections	2.0	330
Laplacians (1 CPU)	38	4,600
Laplacians (12 CPUs)	22	750
Solve F	25	540
Point transfer	5.0	120
Direction transfer	11	260
Gradient transfer	7.0	200

4.2. Point transfer

To test the accuracy of point transfer, we transferred the nodal points of a source mesh onto a destination mesh and back. This let us perform a test for which we knew the ground truth. The exact sequence was $\mathbf{X}^S \rightarrow \mathbf{x}^\mathbf{D} \rightarrow \mathbf{X}^\mathbf{D} \rightarrow \mathbf{x}^\mathbf{S}$ where $\mathbf{X}$ is a point in UVC, $\mathbf{x}$ is a point in Cartesian space, and the superscript refers to the source (S) or destination (D) mesh. Thus, each transfer requires three searches and interpolations as indicated by the mappings. In an ideal transfer, the final result should be the Cartesian coordi-

Table 4
Average error in μm for transferring node locations between meshes. Points were transferred from the source mesh to the destination mesh and back.

Source	Destination mesh			
Mesh	Rabbit-1	Rabbit-2	Canine	Human
Rabbit-1	15.3	28.2	64.3	115
Rabbit-2	38.0	43.2	85.3	115
Canine	97.3	112	126	359
Human	56.8	67.5	192	21.4

Fig. 11. Mapping of the PS across meshes. The PS from the rabbit-1 (left) mesh was mapped to the rabbit-2 (middle) and human (right) meshes.

nates of the source mesh. The average errors for the transfer of all coordinates of all meshes onto all other meshes is presented in Table 4.

The canine mesh produced the largest errors although they were still less than the average edge length of the mesh elements. The self mappings generally performed the best though not always. Part of the error came from linearly interpolating a nonlinear coordinate field. With the human mesh, a weighting function was used for simplicity instead of a much more complicated true linear piecewise interpolation as is used for computation.

4.3. Structural data transfer

To demonstrate the mapping of structural data from one ventricular mesh to another, the PS from rabbit-1 mesh was mapped to the rabbit-2 and human meshes. More specifically, the coordinates of the PS points describing bifurcation nodes, branches, and muscle-junction nodes were converted to UVC on the rabbit-1 mesh and then mapped back to Cartesian coordinates on the other meshes. The results are illustrated in Fig. 11.

The mapping between the rabbit meshes produced a network that was very similar to the original. The human heart geometry is very different from the rabbit so the distances within the PS are distorted on the human mesh but, the topology is maintained.

4.4. Scalar data transfer

In this example, activation times recorded on the ventricular surfaces of an adult male patient were mapped onto the surfaces of the human biventricular mesh. Activation times were obtained with the RHYTHMIA HDx mapping system (Boston Scientific Corporation) at 33,420 points spread out unevenly over the endocardia and epicardium. In this case, UVC were created only for the $\rho = 0$ and $\rho = 1$ surfaces. The activation times from the patient were then transferred with all the features preserved onto the human ventricular mesh. See Fig. 12.

4.5. Vector data transfer

To test how well our UVC algorithm works for transferring directional data between biventricular meshes, we assigned rule-based cardiac fiber orientation to each biventricular mesh using the methods and default parameters in Bayer et al. (2012). For testing purposes, we considered only the longitudinal fiber direction.

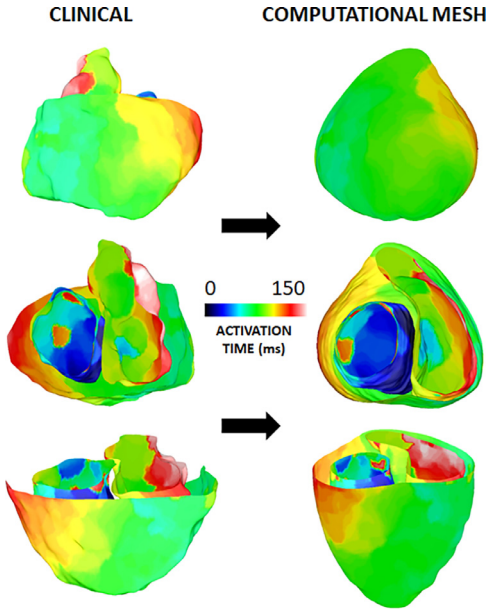

Fig. 12. Activation times from patient ventricles (left column) mapped to the human biventricular mesh (right column). The rows show from top to bottom the inferior, superior, and lateral views of the two hearts oriented in same manner.

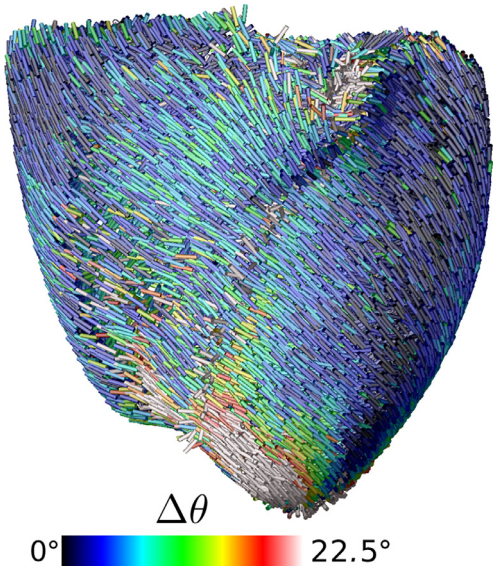

Fig. 13. Anterior view of fibers transferred from the rabbit-1 to human meshes. The color of the vectors indicate the difference with the fibers computed directly on the human mesh. Differences are greatest along the LV-RV junction and at the apex.

To assess error, we computed the angle between the mapped fibers and the rule-based fibers computed directly on the target mesh. For transferring fibers from rabbit-1 to rabbit-2 (see Fig. 13), the average difference in angle over the entire ventricles was 13.2°, but this was not evenly distributed. The greatest differences were clearly near the LV-RV junction where fiber angles changed rapidly over very small distances. The other areas where the error was greatest were the apex and the base. Looking at the LV midwall for example, the differences were less 5°. Transferring from rabbit-2 fibers to canine resulted in a 17.5° average difference, and going the other way resulted in a 25.7° average difference. It is worth noting that starting with a finer mesh resolution leads to a better correspondence. Also, the rule-based method utilized for this study orients fibers at the center of each mesh element based on solutions to Laplace's equation. Thus, differences will exist between the

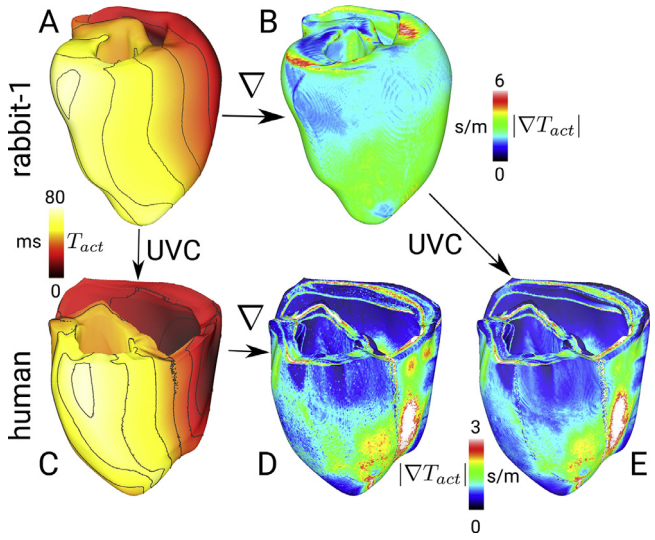

Fig. 14. Gradient transfer from the rabbit-1 mesh to the human mesh. The original activation times in the rabbit-1 mesh with 10 ms isochrones are shown in (**A**). These activation times were then transferred to the human mesh in (**C**), and the gradient computed (**D**). Alternatively, gradients of the original activation times were computed on the rabbit-1 mesh (**B**) and then transferred to the human mesh (**E**). The magnitude of the gradients are shown in B, D, and E.

mapped and directly computed fiber fields since the latter is dependent on the mesh resolution, especially if the mesh is not well discretized in regions of rapid change.

4.6. Gradient transfer

To verify gradient transfer, an electrophysiological simulation was performed with the rabbit-1 mesh stimulated in the RV free wall to produce an activation time map (see Fig. 14). The gradient of the activation times (the inverse of the velocity field) was computed and then the gradient transferred to the human mesh by making use of the deformation gradient. For comparison, the activation times were transferred directly to the human mesh via UVC scalar data transfer, and then the gradient computed for these directly mapped activation times. In theory, the gradients for each method should be the same. However, the gradients on the human mesh did not resemble those on the rabbit-1 mesh since the geometries were quite different. As expected, the gradient was of lower magnitude on the larger heart since the same changes in activation time occurred over a greater spatial distance. Major features are common between both of the human mesh gradients. They were of similar magnitudes and show the same intensity patterns. Differentiating adds noise to signals, so it is not surprising that there were differences, but these were generally small. Further discrepancies were attributable to the differences in mesh resolutions used to compute the gradients. The average difference in gradient direction as computed by the two methods was 7.78° with the errors concentrated at the LV-RV interface.

5. Discussion

We presented universal ventricular coordinates which can be applied to biventricular hearts for the purpose of mapping scalar, vector, and tensor data across different hearts. The UVC algorithm relies on a volumetric mesh and appropriate segmentation. We quantified error associated with the technique using working examples in three dimensions. The results are discussed below.

5.1. Algorithm features

In comparison with other mapping methods, it is computationally quicker and more intuitive to assign coordinates. The process to determine UVC requires little user input and took less than 20 minutes to complete for the largest mesh when using 12 CPUs. For the mappings in this study, the run time was on the order of several minutes, even for the most complex mappings, like gradient transfers which require inverting a 3x3 matrix and performing two 3x3 matrix vector multiplications for every point in the mesh. Run time on a single CPU, even for meshes with over 10 million nodes, was still less than 5 minutes. This is an embarrassingly parallel problem, meaning that computations are independent for each transfer point. So a massive parallelization of this approach could further reduce computation time down to the order of seconds. Although we have demonstrated this technique on unstructured meshes, it would work equally well, if not better, on structured grids since searching is simpler.

A particularly strong demonstration of the method was the gradient transfer. This involved pulling the gradient computed on one mesh to the UVC reference frame using deformation gradients, and then pushing the gradient to a second mesh using an independently calculated deformation gradient. The accuracy of this was verified by transferring the scalar data onto the second mesh and differentiating without using a deformation gradient. Visually, the two gradient patterns are similar.

Clinical data is sometimes incomplete, which is usually the result of either noisy or missing data. UVC may still be computed in this case by assigning the appropriate boundary conditions along the cut surface of the heart. This is exactly why we chose the coordinates to be intuitive, because they can be easily approximated and assigned by eye. Thus, if the apex is omitted for example, the $\hat{z}$ can be set as 0.1 on the bottom edge of the cut mesh instead of 0. Likewise, a small wedge-shaped region of the septum, as used in electrophysiological experimental preparations, is easily defined by ranges in the UVC, e.g., $(0.2 \leq \mathfrak{z} \leq 0.7, 0 \leq \rho \leq 1, -0.2\pi \leq \phi \leq 0.2\pi)$.

5.2. Applications

This UVC algorithm has many applications with a few of them listed here. Generally, the UVC algorithm performs well with meshes of any resolution, but higher resolution meshes yield the most accurate results.

Experimentally describing position: Whole organ electrophysiological studies can be inexact when describing position in or the portion of a heart from which a piece of tissue has been excised. UVC can be estimated by eye and more precisely relay geometrical positioning information in a uniform manner.

Structural data transfer: This method is less prone to mesh degeneration since relative spatial positioning is preserved, which means that mesh elements are less susceptible to collapse. Thus, it is useful to transfer objects between meshes such as scars, vasculature, and the PS.

Scalar field transfer: Transferring scalar data between meshes with UVC is straightforward and robust. A real strength of the UVC algorithm is its ability to transfer data from clinical and experimental measurements directly to biventricular meshes, which is particularly useful for computational studies that model and simulate electrical activation in the heart. For example, activation times recorded at various locations on the heart surfaces, or within the myocardium, can be quickly and accurately transferred to a biventricular mesh. The scalar field transfer with UVC also helps to integrate

data collected with multiple modalities at different spatial resolutions to a single mesh.

Tensor data transfer: Vector data, such as strains by speckle MRI or cardiac fibers from diffusion tensor MRI, are very important to studies investigating the electromechanical behavior of the heart. Transferring tensor data relies on reasonable gradients in the coordinate fields. $\jmath$ was the most well behaved since it varied in a simple fashion and required straight forward boundary conditions. ρ was also reasonably well defined, but depending on the mesh resolution, the area near the LV-RV interfaces could experience drastic changes across one or two elements. ν showed two discontinuities at ± 1 which could lead to discrepancies in those regions.

Gradient field transfer and deformation: Local changes between two meshes can be quantified by looking at local deformation gradients, F. Given mesh a with F^a and mesh b with F^b, the deformation gradient between meshes is $F^a F^{-b}$. This can be applied to quantify changes during the cardiac cycle, or changes of heart geometry as a disease progresses.

Rule-based assignment: The UVC algorithm generates smoothly varying functions throughout the heart which are useful for rule-based definitions of structures and properties. For example, they are useful for determining rule-based fiber orientation (Bayer et al., 2012), as well as to accurately assign experimentally derived electrophysiological properties throughout the myocardium to generate a realistic ECG (Keller et al., 2012). By applying such properties in a biventricular mesh in a smooth manner throughout the LV, RV, septum, and their junctions, numerical artifacts in computer simulations from discontinuities in the model are minimized.

5.3. Patient-specific cardiac structures

Besides the trabeculae and valve openings mentioned earlier, papillary muscles and the moderator band are two other specialized anatomical structures which differ in topology and location. However, they also differ in quantity which makes assigning unique UVC without special treatment impossible. Here we discuss possible extensions to the UVC approach to handle each unique patient-specific cardiac structure.

5.3.1. Moderator band

The moderator band extends from the septum to the base of the free wall of the RV where it attaches to the base of a papillary muscle. A Purkinje fiber runs within the moderator band and is isolated from the surrounding myocardial sheath. The moderator band's structure, length, width, and attachment points are highly variable between individuals. Since it is without a fixed topology, we chose not to include it in our generalized UVC algorithm. However, the endocardial points of attachment to the endocardium can be specified with UVC. At the points of attachment, a local cylindrical coordinate system for the long axis of the moderator band can be constructed using the normalized distance from the septum to the RV wall. Then with respect to this axis, an angle and radius can be calculated to uniquely identify position within the short axis of the moderator band.

5.3.2. Papillary muscles

Papillary muscles play an important role in heart valve function. However, their quantity and location vary from heart to heart. Additionally, for each muscle there are variable numbers of attachments between the muscle and the endocardium. This makes a unique mapping of papillary muscles between hearts with UVC impossible. As done with the moderator band, the base of a papillary muscle and its points of attachment can be described using the $\jmath$ and ϕ coordinates, and the ρ can be modified to parameterize the distance between these attachments with the tip of the papillary muscle. Likewise, an angle and radius can be calculated with respect to this long axis of the papillary muscle to determine position within its short axis. However, this would need to be repeated for each papillary muscle.

A more robust approach would be to map patient-specific endocardial topology from high resolution data sources to the endocardium of smooth meshes. Specifically, UVC could be determined for the reference points in Figs. 5 and 7 of Paun et al. (2017) for any of the meshes used in this study. Then their high resolution endocardial structures could be easily mapped between our meshes parameterized with UVC.

5.4. Limitations

Distance measured in UVC and Cartesian coordinates is not equal. Thus, scaling is required to improve searching so that distance along a coordinate in UVC, which changes more or less rapidly than in Cartesian space, is not overly weighted, especially ρ. The empirically found overall optimal scaling agreed well with the theoretical considerations. Nodes were correctly identified in the proper element 99% of the time. Some target nodes, especially those on the surface of one mesh, may not be found within the elements of another mesh since smooth surfaces are represented by linear elements with planar faces tangent to the true surface. Transferring points to one mesh and back produced average errors that were much less than the edge length of the elements. This identity mapping was an extreme test as 3 transfers had to be performed and errors accumulated with each transform. Nonetheless, accuracy was acceptable for the minimal computational costs.

The coordinates ϕ, ρ, and ν are discontinuous at the LV-RV junction. This may introduce localized errors at the LV-RV junction when mapping scalar, vector, and tensor data between biventricular meshes. Since this junction is easy to define in UVC, a simple smoothing operator could be applied to the LV-RV junction in the mappings to minimize these errors.

6. Conclusion

The UVC algorithm maps position within the ventricles of hearts to a generic frame of reference based on Laplacian solutions. This allows for the efficient transfer of data between different hearts with high accuracy. The UVC algorithm handles data from many different sources in the form of scalar, vector, and tensor quantities. The computational demands are insignificant compared to alternative methods.

Acknowledgments

The authors would like to acknowledge Dr. Martin Bishop for providing the OxRabHi and OxRabLo meshes.

This work was funded in part by the Agence Nationale de Recherche (ANR) as part of the Investissements d'Avenir program, grant ANR-10-IAHU-04. J.Bayer was supported in part by the ANR grant ANR-16-CE19-0009, the Whitaker International Program administered by the Institute of International Education, and by the Lefoulon-Delalande Foundation administered by the Institute of France. A. Pashaei was supported by the ANR grant ANR-13-MONU-0004-02. Funding to G Plank was provided by the grants F3210-N18 and I2760-B30 from the Austrian Science Fund (FWF) and the EU grant CardioProof 611232. E. Vigmond and G. Plank were also supported by the ERACoSysMed PUSHCART project. Simulations for this study were performed on the high performance computing

platform Avakas, which is maintained by the Mesocentre de Calcul Intensif Aquitain (MCIA). We would also like to acknowledge PRACE support for computations performed on Marconi@CINECA, Italy and ARCHER, UK.

References

Bayer, J.D., Blake, R.C., Plank, G., Trayanova, N.A., 2012. A novel rule-based algorithm for assigning myocardial fiber orientation to computational heart models. Ann. Biomed. Eng. 40 (10), 2243–2254. doi:10.1007/s10439-012-0593-5.

Bayer, J.D., Lalani, G.G., Vigmond, E.J., Narayan, S.M., Trayanova, N.A., 2016. Mechanisms linking electrical alternans and clinical ventricular arrhythmia in human heart failure. Heart Rhythm 13, 1922–1931. doi:10.1016/j.hrthm.2016.05.017.

Beg, M., Miller, M., Trouvé, A., Younes, L., 2005. Computing large deformation metric mappings via geodesic flows of diffeomorphisms. Int. J. Comput. 61, 139–157.

Bishop, M.J., Plank, G., 2012. The role of fine-scale anatomical structure in the dynamics of reentry in computational models of the rabbit ventricles. J. Physiol. (Lond.) 590, 4515–4535. doi:10.1113/jphysiol.2012.229062.

Bishop, M.J., Plank, G., Burton, R.A.B., Schneider, J.E., Gavaghan, D.J., Grau, V., Kohl, P., 2010. Development of an anatomically detailed mri-derived rabbit ventricular model and assessment of its impact on simulations of electrophysiological function. Am. J. Physiol. Heart Circ. Physiol. 298, H699–H718. doi:10.1152/ajpheart.00606.2009.

Cerqueira, M.D., Weissman, N.J., Dilsizian, V., Jacobs, A.K., Kaul, S., Laskey, W.K., Pennell, D.J., Rumberger, J.A., Ryan, T., Verani, M.S., American Heart Association Writing Group on Myocardial Segmentation and Registration for Cardiac Imaging, 2002. Standardized myocardial segmentation and nomenclature for tomographic imaging of the heart. a statement for healthcare professionals from the cardiac imaging committee of the council on clinical cardiology of the american heart association. Int. J. Cardiovasc. Imaging 18 (1) 539-42.

Costa, K.D., Hunter, P.J., Wayne, J.S., Waldman, L.K., Guccione, J.M., McCulloch, A.D., 1996. A three-dimensional finite element method for large elastic deformations of ventricular myocardium: ii - prolate spheroidal coordinates. J. Biomech. Eng. 118 (4), 464–472.

Eriksson, T.S.E., Prassl, A.J., Plank, G., Holzapfel, G.A., 2013. Influence of myocardial fiber/sheet orientations on left ventricular mechanical contraction. Math. Mech. Solids 18 (6), 592–606.

Janse, M.J., Coronel, R., Opthof, T., Sosunov, E.A., Anyukhovsky, E.P., Rosen, M.R., 2012. Repolarization gradients in the intact heart: transmural or apico-basal? Prog. Biophys. Mol. Biol. 109 (1–2), 6–15. doi:10.1016/j.pbiomolbio.2012.03.001.

Jones, E., Oliphant, T., Peterson, P., et al., 2001. SciPy: Open source scientific tools for Python.

Keller, D.U.J., Weiss, D.L., Dossel, O., Seemann, G., 2012. Influence of i(ks) heterogeneities on the genesis of the t-wave: a computational evaluation. IEEE Trans. Biomed. Eng. 59 (2), 311–322. doi:10.1109/TBME.2011.2168397.

Lou, Q., Fedorov, V.V., Glukhov, A.V., Moazami, N., Fast, V.G., Efimov, I.R., 2011. Transmural heterogeneity and remodeling of ventricular excitation-contraction coupling in human heart failure. Circulation 123 (17), 1881–1890. doi:10.1161/CIRCULATIONAHA.110.989707.

Maneewongvatana, S., Mount, D.M., 2001. On The Efficiency of Nearest Neighbor Searching with Data Clustered in Lower Dimensions. Springer.

Miller, M.I., Younes, L., Trouvé, A., 2014. Diffeomorphometry and geodesic positioning systems for human anatomy. Technol. (Singap World Sci) 2 (1), 36. doi:10.1142/S2339547814500010.

Moreno, J.D., Zhu, Z.I., Yang, P.-C., Bankston, J.R., Jeng, M.-T., Kang, C., Wang, L., Bayer, J.D., Christini, D.J., Trayanova, N.A., Ripplinger, C.M., Kass, R.S., Clancy, C.E., 2011. A computational model to predict the effects of class i anti-arrhythmic drugs on ventricular rhythms. Sci. Transl. Med. 3 (98), 98ra83. doi:10.1126/scitranslmed.3002588.

Morita, S.T., Zipes, D.P., Morita, H., Wu, J., 2007. Analysis of action potentials in the canine ventricular septum: no phenotypic expression of m cells. Cardiovasc. Res. 74 (1), 96–103. doi:10.1016/j.cardiores.2007.01.003.

Pandit, S.V., Kaur, K., Zlochiver, S., Noujaim, S.F., Furspan, P., Mironov, S., Shibayama, J., Anumonwo, J., Jalife, J., 2011. Left-to-right ventricular differences in i(katp) underlie epicardial repolarization gradient during global ischemia. Heart Rhythm 8 (11), 1732–1739. doi:10.1016/j.hrthm.2011.06.028.

Paun, B., Bijnens, B., Iles, T., Iaizzo, P.A., Butakoff, C., 2017. Patient independent representation of the detailed cardiac ventricular anatomy. Med. Image Anal. 35, 270–287. doi:10.1016/j.media.2016.07.006.

Plank, G., Burton, R.A.B., Hales, P., Bishop, M., Mansoori, T., Bernabeu, M.O., Garny, A., Prassl, A.J., Bollensdorff, C., Mason, F., Mahmood, F., Rodriguez, B., Grau, V., Schneider, J.E., Gavaghan, D., Kohl, P., 2009. Generation of histo-anatomically representative models of the individual heart: tools and application. Philos. Trans. A Math. Phys. Eng. Sci. 367, 2257–2292. doi:10.1098/rsta.2009.0056.

Plank, G., Liebmann, M., Weber dos Santos, R., Vigmond, E.J., Haase, G., 2007. Algebraic multigrid preconditioner for the cardiac bidomain model. IEEE Trans. Biomed. Eng. 54, 585–596. doi:10.1109/TBME.2006.889181.

Potse, M., Dubé, B., Richer, J., Vinet, A., Gulrajani, R.M., 2006. A comparison of monodomain and bidomain reaction-diffusion models for action potential propagation in the human heart. IEEE Trans. Biomed. Eng. 53 (12 Pt 1), 2425–2435. doi:10.1109/TBME.2006.880875.

Sabir, I.N., Killeen, M.J., Goddard, C.A., Thomas, G., Gray, S., Grace, A.A., Huang, C.L.-H., 2007. Transient alterations in transmural repolarization gradients and arrhythmogenicity in hypokalaemic Langendorff-perfused murine hearts. J. Physiol. 581 (Pt 1), 277–289. doi:10.1113/jphysiol.2007.128637.

Streeter Jr., D., Spotnitz, H.M., Patel, D.P., Ross, JrJ., Sonnenblick, E.H., 1969. Fiber orientation in the canine left ventricle during diastole and systole. Circ. Res. 24 (3), 339–347.

Vadakkumpadan, F., Arevalo, H., Ceritoglu, C., Miller, M., Trayanova, N., 2012. Image-based estimation of ventricular fiber orientations for personalized modeling of cardiac electrophysiology. IEEE Trans. Med. Imaging 31 (5), 1051–1060. doi:10.1109/TMI.2012.2184799.

Vetter, F.J., McCulloch, A.D., 1998. Three-dimensional analysis of regional cardiac function: a model of rabbit ventricular anatomy. Prog. Biophys. Mol. Biol. 69, 157–183.

Volders, P.G., Sipido, K.R., Carmeliet, E., Spätjens, R.L., Wellens, H.J., Vos, M.A., 1999. Repolarizing k+ currents ito1 and iks are larger in right than left canine ventricular midmyocardium. Circulation 99 (2), 206–210.